Nampt activator P7C3 ameliorates diabetes and improves skeletal muscle function modulating cell metabolism and lipid mediators

Ravikumar Manickam[1], Jared Tur[1], Sachin L. Badole[1], Kalyan C. Chapalamadugu[1], Puja Sinha[1], Zhiying Wang[2], David W. Russ[3], Marco Brotto[2]* & Srinivas M. Tipparaju[1]*

[1]*Department of Pharmaceutical Sciences, Taneja College of Pharmacy, University of South Florida, Tampa, FL, USA;* [2]*Bone-Muscle Research Center, College of Nursing & Health Innovation, University of Texas-Arlington (UTA), Arlington, TX, USA;* [3]*School of Physical Therapy and Rehabilitation Sciences, Morsani College of Medicine, University of South Florida, Tampa, FL, USA*

Abstract

Background Nicotinamide phosphoribosyltransferase (Nampt), a key enzyme in NAD salvage pathway is decreased in metabolic diseases, and its precise role in skeletal muscle function is not known. We tested the hypothesis, Nampt activation by P7C3 (3,6-dibromo-α-[(phenylamino)methyl]-9H-carbazol-9-ethanol) ameliorates diabetes and muscle function.
Methods We assessed the functional, morphometric, biochemical, and molecular effects of P7C3 treatment in skeletal muscle of type 2 diabetic (*db/db*) mice. Nampt$^{+/-}$ mice were utilized to test the specificity of P7C3.
Results Insulin resistance increased 1.6-fold in diabetic mice compared with wild-type mice and after 4 weeks treatment with P7C3 rescued diabetes ($P < 0.05$). In the db-P7C3 mice fasting blood glucose levels decreased to 0.96-fold compared with C57Bl/6J wild-type naïve control mice. The insulin and glucose tolerance tests blood glucose levels were decreased to 0.6-fold and 0.54-folds, respectively, at 120 min along with an increase in insulin secretion (1.76-fold) and pancreatic β-cells (3.92-fold) in db-P7C3 mice. The fore-limb and hind-limb grip strengths were increased to 1.13-fold and 1.17-fold, respectively, together with a 14.2-fold increase in voluntary running wheel distance in db-P7C3 mice. P7C3 treatment resulted in a 1.4-fold and 7.1-fold increase in medium-sized and larger-sized myofibres cross-sectional area, with a concomitant 0.5-fold decrease in smaller-sized myofibres of tibialis anterior (TA) muscle. The transmission electron microscopy images also displayed a 1.67-fold increase in myofibre diameter of extensor digitorum longus muscle along with 2.9-fold decrease in mitochondrial area in db-P7C3 mice compared with db-Veh mice. The number of SDH positive myofibres were increased to 1.74-fold in db-P7C3 TA muscles. The gastrocnemius and TA muscles displayed a decrease in slow oxidative myosin heavy chain type1 (MyHC1) myofibres expression (0.46-fold) and immunostaining (6.4-fold), respectively. qPCR analysis displayed a 2.9-fold and 1.3-fold increase in *Pdk4* and *Cpt1*, and 0.55-fold and 0.59-fold decrease in *Fgf21* and 16S in db-P7C3 mice. There was also a 3.3-fold and 1.9-fold increase in *Fabp1* and *CD36* in db-Veh mice. RNA-seq differential gene expression volcano plot displayed 1415 genes to be up-regulated and 1726 genes down-regulated ($P < 0.05$) in db-P7C3 mice. There was 1.02-fold increase in serum HDL, and 0.9-fold decrease in low-density lipoprotein/very low-density lipoprotein ratio in db-P7C3 mice. Lipid profiling of gastrocnemius muscle displayed a decrease in inflammatory lipid mediators n-6; AA (0.83-fold), and n-3; DHA (0.69-fold) and EPA (0.81-fold), and a 0.66-fold decrease in endocannabinoid 2-AG and 2.0-fold increase in AEA in db-P7C3 mice.
Conclusions Overall, we demonstrate that P7C3 activates Nampt, improves type 2 diabetes and skeletal muscle function in db/db mice.

Keywords P7C3; Nampt; Skeletal muscle; Insulin sensitivity; Physical performance; Pathophysiology

Introduction

Type 2 diabetes mellitus is one of the most common and chronic metabolic disease worldwide.[1] Type 2 diabetes has a debilitating impact on the whole body with major changes affecting the musculoskeletal system. It is mainly characterized by insulin resistance with the inability of the metabolic tissues such as skeletal muscle and liver to utilize insulin for maintaining glucose homeostasis, resulting in elevated blood glucose levels leading to hyperglycaemia.[2,3] The occurrence of type 2 diabetes has increased rapidly in the last few decades and is the 7th major cause of mortality in the USA (CDC, USA). There is increased prevalence of type 2 diabetes in younger population due to obesity, which is a predisposing factor to the metabolic disease.[4] Due to an increase in the number of older populations, the incidence of type 2 diabetes has also increased worldwide.[5] Type 2 diabetes is a major cause of cardiovascular diseases and neurodegenerative disorders.[6,7] Diabetes affects skeletal muscle mass, strength and function through impaired energy metabolism, decreased blood flow, mitochondrial dysfunction and cell death.[8]

Skeletal muscle is a major metabolic organ that not only utilizes glucose to produce the energy needed for contraction but also plays a key role in insulin-stimulated glucose uptake in the postprandial state, and overall energy expenditure in mammals.[9,10] Thus, skeletal muscle insulin resistance plays an important role in the pathophysiology of type 2 diabetes even before the pancreatic β cells dysfunction and the development of overt hyperglycaemia.[11] Disruption of key insulin signalling pathways prevents the normal utilization of circulating blood glucose and storage of excess glucose as glycogen in the muscle and liver leading to hyperglycaemia and insulin resistance.[12] Further, the secretion of pro-inflammatory cytokines by immune cells and the increase in lipolysis and free fatty acids, and the accumulation of intermediary lipid metabolites from other tissues such as adipose tissue can induce myocyte inflammation in obesity and negatively regulate the muscle cell metabolism resulting in insulin resistance.[3] The skeletal muscle inflammation is also caused by the ectopic fat deposition, that is, inter-muscular and intra-muscular lipid accumulation and can add to the degree of insulin resistance through paracrine effects.[13] In addition, mitochondrial dysfunction has also been attributed in the development of insulin resistance and type 2 diabetes.[14]

Nampt is a key rate-limiting enzyme in the NAD salvage pathway, which is dysregulated in the metabolic disease such as diabetes, and during ageing.[15–19] Nampt is ubiquitously expressed, and the homozygous-null genotype is embryonically lethal in mice.[20] Muscle-specific knockdown of Nampt in mice reduces the intramuscular NAD^+ levels and causes myofibre degeneration and loss of physical functions like strength and endurance capacity mimicking type 2 diabetes in humans.[21] Furthermore, knockdown of Nampt in mouse C2C12 myoblasts also reduces the NAD^+ levels and results in decreased mitochondrial biogenesis.[22] The Nampt activator, P7C3 was initially identified as a neuroprotective aminopropyl carbazole agent, which binds to and enhances the Nampt activity.[23,24] However, the precise role of Nampt in skeletal muscle function and pathophysiology of metabolic disease such as type 2 diabetes is not known. In the present study, we hypothesized that P7C3-mediated Nampt activation in the *db/db* mouse model of type 2 diabetes ameliorates the skeletal muscle diabetic phenotype and improves insulin sensitivity and function.

Methods

Animals

The C57Bl/6J wild-type (WT), and the type 2 diabetic B6.BKS (D)-Lepr^{db}/J (*db/db*) male mice were purchased from Jackson laboratories. The Nampt heterozygous (Nampt$^{+/−}$) mice were provided by Dr. Junichi Sadoshima (Rutgers Medical School, NJ, USA), and the colonies were bred and maintained at the Morsani College of Medicine, University of South Florida, USA. The 16-weeks old male *db/db* mice were treated with Nampt activator, P7C3 (db-P7C3) (10 mg/kg body weight for 4 weeks, daily, i/p). The vehicle control *db/db* (db-Veh) mice were treated with an equivalent dose of DMSO dissolved in 10% Kolliphor oil (Sigma-Aldrich, MO, USA) in phosphate buffered saline (PBS). The age-matched C57Bl/6J WT male mice were used as naïve control. In addition, 20–24 weeks old Nampt heterozygous (Nampt$^{+/−}$) and their littermate WT male mice were also treated with Nampt activator, 10 mg/kg body weight P7C3 (P7C3) once, i/p. The vehicle control Nampt$^{+/−}$ (vehicle) male mice were treated with an equivalent dose of DMSO dissolved in 10% Kolliphor oil in

phosphate buffered saline (PBS). A total of 156 mice were used in this study, that is, 50 db-Veh and 51 db-P7C3 treated mice, and 35 C57Bl/6J WT and 10 each of the Nampt$^{+/-}$ and littermate WT mice. All mice used in this study were fed with food and water *ad libitum*. All animal work was approved before start of the study by the Institutional Animal Care and Use Committee at the University of South Florida, Tampa, FL, USA.

Fasting blood glucose and serum lipids

Mice were fasted 6 h, and tail vein blood was used for glucose measurement with ACCU-CHECK blood glucose meter (Roche Diagnostics, Mannheim, Germany) on a weekly basis for 4 weeks. At the end of 4 week treatment, blood was collected by retro orbital plexus technique for the assessment of serum lipids content using the Rat/Mouse Insulin ELISA kit (Millipore, MA, USA) following manufacturer's instructions. The serum high-density lipoprotein (HDL) and low-density lipoprotein/very low-density lipoprotein (LDL/VLDL) were quantified using HDL and LDL/VLDL quantification kit (Sigma-Aldrich, MO, USA USA).

Insulin tolerance test

Both db-Veh and db-P7C3 mice were fasted for 6 hours and were injected with a single dose of 1 U/kg body weight Novolin R regular human Insulin (Novo Nordisk, NJ, USA), i/p for the insulin tolerance test (ITT). The blood glucose levels were measured at 0, 30, 60, 90 and 120 min after the administration of human insulin with ACCU-CHEK glucose analyser (Roche Diagnostics, Mannheim, Germany).

Glucose tolerance test

The glucose tolerance test (GTT) was performed in the Lepr$^{-/-}$ (*db/db*) and Nampt$^{+/-}$ mice. After 4 weeks of treatment, both the db-Veh and db-P7C3 treated mice were fasted overnight for GTT assay. GTT was performed by a single dose of intraperitoneal injection of 2 g/kg body weight of D-(+)-glucose (Sigma-Aldrich, MO, USA). Blood samples were obtained by the retro orbital plexus technique. Serum glucose levels were determined prior to glucose administration (0 min) and after 30, 60, 90, and 120 min of glucose injection, using glucose oxidase peroxidase kit (Pointe Scientific Inc., MI, USA) and following manufacturer's instructions. Similarly, the Nampt$^{+/-}$ and their littermate WT mice were fasted overnight and given a single dose of vehicle control or P7C3 30 min prior to the administration of 2 g/kg body weight D-(+)-glucose, i/p. The circulating blood glucose levels were measured with ACCU-CHECK blood glucose meter at 0, 15, 30, 60, 120 minutes of glucose admin-

istration. The index of the total glucose shift was calculated as the area under the curve (AUC) using trapezium method.

Immunostaining

Immunostaining of the pancreas was performed for the measurement of insulin secreting β cells area, as previously described.[25] Briefly, the frozen pancreatic tissues were fixed into tissue freezing media (TFM). Pancreas were cut into 10 μm thick sections and kept at −80°C. For immunostaining, the slides were first air dried and washed with phosphate buffer saline (PBS). The sections were then fixed in 4% paraformaldehyde for 30 min and blocked with SuperBlock™ T20 (TBS) blocking buffer (Thermo scientific, MA, USA) for 30 min, at room temperature (RT). Slides were then incubated with insulin primary antibody (sc-9168, Santa Cruz, TX, USA) diluted in blocking buffer (1:200), overnight at 4°C. Slides were then washed in PBS and incubated with Alexa Fluor®488 secondary antibody (Abcam, MA, USA) diluted in blocking buffer for 1 h at RT. Following washes, the slides were then mounted with ProLong® Gold antifade mountant containing DAPI (Molecular Probe, OR, USA). Nuclei were labelled by DAPI. The images obtained with confocal multiphoton laser scanning microscope (Olympus FV1000 MPE, Olympus Inc., USA) were quantified by using ImageJ software (NIH, USA). The cross-sectional areas of pancreas and β cells were determined from multiple sections (*n* = 3 mice per group), separated by at least 50 μm from each section. Pancreatic β cell area was calculated by using the following formula: islet β cell area (%) = (area stained by insulin antibody/total islets area) × 100.

Gomori aldehyde fuchsin staining

The Gomori aldehyde fuchsin staining of the pancreatic β cells was performed as per previously published protocol.[26] Briefly, the frozen pancreas was TFM embedded and cut into 6 μm thick transverse serial cryosections using Microm cryostat machine. The slides were air dried at 60°C and dewaxed using xylene and then hydrated through decreasing concentrations of ethyl alcohol. The slides were then rinsed in cold tap water followed by a single rinse in 50% ethanol and immersed in aldehyde fuchsin (Electron Microscopy Services, PA, USA) for 1 h. The excess stain was removed by rinsing in 70% ethanol and tap water. The slides were then counter-stained with Light Green (American Master Tech Scientific, CA, USA) through immersion for 60 s and dehydrated with increasing concentration of ethanol, and cleared with xylene. The sections were then mounted with disterene phthalate xylene (DPX) mountant (Sigma-Aldrich, MO, USA). Images were obtained at ×20 magnification with

the Olympus IX73 inverted microscope using CellSens Standard software (Olympus Soft Imaging Solution, USA) and quantified with ImageJ software (NIH, USA).

Grip strength and voluntary running wheel

The fore-limb and hind-limb grip strengths were measured with the use of Chatillon force measurement DFE II grip strength meter (Ametek, Columbus Instruments, OH, USA). The average of five measurements per mice is represented as KGF/kg body weight for both the fore-limb and hind-limb grip strengths measured. The overnight voluntary running wheel experiments were carried out with the Columbus Instruments 0297, the CI Multi-Device Interface (Columbus Instruments, OH, USA) per manufacturer's recommendations.

Ex vivo myofibre contractility and force-frequency relationship

Animals were euthanized in compliance with University of South Florida IACUC guidelines. The extensor digitorum longus (EDL) muscles of each animal were tied with surgical silk at the proximal and distal tendons and dissected free. Muscles were immediately transferred to a customized vertical organ bath system (Aurora Scientific Inc., Canada) with the suture on the distal tendon clamped in place and that on the proximal tendon tied to a force transducer such that the muscles were positioned between two platinum wire stimulating electrodes. The buffer (137 mM NaCl, 0.4 mM NaH_2PO_4, 5.1 mM KCl, 1.05 mM $MgCl_2$, 2.0 mM $CaCl_2$ and 10 mM glucose; pH 7.4) in the bath was maintained at 22°C and continuously aerated with 95%/5% O_2/CO_2. Muscles were equilibrated for 10–15 min after which, the optimal muscle length (l_O) for each muscle was calculated by adjusting the length until a maximal force response to a single twitch was attained. Following determination of l_O, the muscles were subjected to stimulation trains (500 ms duration) of frequencies ranging from 1–125 Hz, 1 per minute to determine the force-frequency relationship (FFR). Stimulation was delivered with a S8800 dual pulse digital stimulator (Grass Products, West Warwick, RI, USA), and all pulses were 1 ms in duration. The peak forces of each contraction at the different stimulation frequencies were used to plot the FFR. Muscle force was expressed in both absolute (mN) and normalized terms (mN/mg muscle mass) of myofibre FFR. n = 5–6 EDL muscles from three mice per group.

Haematoxylin and eosin staining

The tibialis anterior (TA) muscle was dissected from the mice, and embedded in optimal cutting temperature (OCT), frozen

in isopentane chilled in liquid nitrogen and stored at −80°C. The 10 μm thick transverse serial cryosections were cut at the mid-belly region using Microm cryostat machine, and stained with haematoxylin and eosin[27] for the analysis of myofibre cross-sectional area of the WT, db-Veh and db-P7C3 treated mice. Images were obtained at ×10 and ×20 magnifications with the Olympus IX73 inverted microscope and were quantified using CellSens Standard software (Olympus Soft Imaging Solution, USA).

Transmission electron microscopy

The EDL muscles were fixed with 2.5% glutaraldehyde in 0.1 M sodium phosphate buffer for 2 h at RT, and overnight at 4°C, followed by washing in buffer and fixation with 1% osmium tetroxide in buffer for 2 h at 4°C. After rinsing in buffer, the samples were then dehydrated in ethanol and acetone at RT and infiltrated in acetone: pure resin (Embed812) mix in vacuum with desiccant for 1 h and in pure resin for 4 h and embedded in the embedding mix. Polymerization of the embedding mix was carried out overnight at 70°C in the embedding moulds. Semithin (1 μm) and ultrathin (70 nm) sections were cut using a Reichert Ultracut microtome machine. The sections were then stained with 2% uranyl acetate and contrasted with lead citrate as per standard protocol. Images were taken at ×15 000, ×30 000, and ×50 000 magnifications with a JOEL1400 transmission electron microscope for the analysis of myofibre diameter and the mitochondrial area.

Mitochondrial DNA (mtDNA) copy number

Total DNA was extracted from gastrocnemius (GAS) muscle using DNeasy Blood and Tissue kit (Qiagen, MD, USA) according to the manufacturer's protocol. The quantitative real-time PCR (qPCR) analysis of the mtDNA/nDNA was performed using iTaq Universal SYBR green supermix (Bio-Rad Laboratories, CA, USA). The mouse 16S was used as the mitochondrial gene and HK2 was used as the nuclear gene to obtain the mitochondrial copy number.

Succinate dehydrogenase staining

The 10 μm thick transverse cryosections of TA muscles were cut at the mid-belly region using Leica CM 1860 AgProtect cryostat machine. Briefly, the tissue sections were air-dried for 45 minutes, and incubated in 50 mM sodium succinate dibasic hexahydrate and 1.25 mM nitroblue tetrazolium in 0.1 M phosphate buffer (Sigma-Aldrich, MO, USA) for 30 min. The reaction was stopped washing in deionized water, and the sections were dehydrated in a series of graded ethanol and cleared using xylene. The sections were then

mounted with DPX mountant, and the images were captured at ×20 magnification of the Olympus IX73 inverted microscope using CellSens Standard software (Olympus Soft Imaging Solution, USA) and the succinate dehydrogenase (SDH) positive myofibres were quantified with ImageJ software.

Quantitative real-time PCR

Total RNA was isolated from GAS muscle using the Exiqon miRCURY RNA Isolation kit (Exiqon, MA, USA) according to the manufacturer's protocol. Complimentary DNA from total RNA was synthesized with iScript cDNA synthesis kit (Bio-Rad Laboratories, CA, USA) and quantitative real-time PCR (qPCR) analysis was performed on key transcriptome targets using iTaq Universal SYBR Green Supermix (Bio-Rad Laboratories, CA, USA). The cDNA synthesis and qPCR procedures were performed as described previously.[28] The mouse HPRT gene was used as an internal control.

Luminex Magpix IP-10 (C-X-C motif chemokine ligand 10) immunoassay

The serum inflammatory markers were analysed using a mouse cytokine/chemokine antibody-immobilized premixed 32-plex Luminex magnetic beads based 96-Well plate immunoassay kit (Milliplex Map kit—MCYTMAG-70K-PX32, EMD Millipore Corporation, MA, USA) according to the manufacturer's instruction. Briefly, the serum samples were diluted at 1:2 in the assay buffer and measured in duplicates along with the standards and quality controls. The serum samples were incubated overnight at 4°C with the magnetic beads. The wells were then washed with wash buffer and incubated with the detection antibodies for 1 h at RT, followed by a streptavidin-phycoerythrin incubation for 30 min at RT. After washing, the plate was run on MAGPIX with xPONENT software. The mean fluorescent intensity data was analysed using a five-parameter logistic curve-fitting Multi Analyst software for calculating the cytokine/chemokine concentrations of the samples (n = 6 mice per group).

Whole transcriptome sequencing (RNA Seq)

The RNA Seq of GAS muscle was carried out using Novogene Next Generation Sequencing platform NovaSeq 6000 PE150 (Novogene, Sacramento, CA, USA). Total RNA was extracted from GAS muscle and the RNA quality and integrity were determined. RNA Seq library was then prepared and the cDNA library quality were determined before sequencing with Illumina PE150 platform. The data generated were analysed between groups (n = 3 mice/group) for bioinformatics analysis.

Bioinformatic analysis

The Heatmap, Volcano Plot and Venn diagram were generated using R 4.1.1 software for differentially expressed genes. The gene network and pathways were analysed using DAVID v6.8 for GO enrichment analysis with Benjamini significant $P < 0.05$ for both up-regulated and down-regulated genes. The Gene interaction network construction and visualization was performed using Cytoscape v3.8.2.[29,30] The identified treatment responsive differentially expressed genes were created with the Search Tool for the Retrieval of Interacting Genes and proteins (STRING) database. Default settings of confidence score and maximum additional interactors were used for visualization. The Molecular Complex Deletion (MCODE) plugin for Cytoscape was used to identify the network modules.[31] Densely connected regions/clusters in the co-expression network were identified with the following parameters; degree cut-off = 2, haircut, k-core = 2, node score cut off = 0.2 and max. depth = 100.

Myofibre staining

The 10 μm thick transverse serial cryosections of TA muscles were cut at the mid-belly region using Microm cryostat machine. Briefly, the tissue sections were blocked with 0.2% bovine serum albumin (BSA) and 10% normal sheep serum (NSS) in PBS-Triton X100 (PBST) for 1 h at RT. All washes were carried out with PBS. Following washing, the sections were incubated in 5 μg/mL of mouse monoclonal primary antibody against myosin heavy chain type-1 (A4.840s DSHB, IA, USA) in 0.2% BSA and 5% NSS antibody dilution buffer in PBST overnight at 4°C. After washing, the sections were then fixed with 10% neutral buffered formalin for 5 min at RT, washed and incubated in 1:300 dilution of biotinylated sheep anti-mouse IgG (ab6807, Abcam, MA, USA) and 1:1000 dilution of rabbit anti-laminin (L9393, Sigma-Aldrich, MO, USA) in the antibody dilution buffer for 1 h at RT. Following washes, the tissue sections were then incubated in 1:400 dilution of streptavidin AF488 conjugate and goat anti-rabbit AF594 (Invitrogen, CA, USA) and then washed and mounted with Prolong gold anti-fade mounting medium with DAPI (Invitrogen, CA, USA). Images were obtained at ×10 and ×20 magnifications with the Olympus IX73 inverted microscope using CellSens Standard software (Olympus Soft Imaging Solution, USA) and the MyHC1 positive myofibres were quantified with ImageJ software.[28]

Lipidomics

The lipidomic profiling of GAS muscle was performed using a liquid chromatography–tandem mass spectrometry (LC—MS/MS) method as described previously.[32,33] Briefly, the

GAS muscle samples were collected, and flash frozen in liquid nitrogen. Around 50–100 mg of the muscle tissue was homogenized using a bead-beating method, then the obtained supernatant was further cleaned and concentrated by solid phase extraction. The extracted LMs samples were dried under vacuum and stored at −80°C for future LC–MS/MS analysis. The dried extracts were reconstituted with 50 μL of methanol, and 10 μL was injected into LC–MS/MS to observe lipid profiles in GAS muscles. The LC–MS/MS system components were from Shimadzu Scientific Instruments Inc. (Columbia, MD, USA). All analyses and data processing were completed with the use of Shimadzu Lab Solutions V5.91 software (Shimadzu Scientific, Tokyo, Japan).

Nampt enzymatic activity

The Nampt enzymatic activity was measured from the GAS muscles of WT naïve control, db-Veh and db-P7C3 treated mice using the commercially available CycLex Nampt Colorimetric Assay Kit (MBL international, MA, USA) as per manufacturer's instructions. The OD values were obtained at 450 nm with the Synergy Hybrid H4 96-Well Plate Reader (Biotek, VT, USA) using Gen5 software after the sample incubation at 30°C, and the Nampt enzymatic activity was assessed.

Serum pyruvate enzymatic activity

Serum pyruvate levels were measured using the pyruvate assay kit (Sigma-Aldrich, MO, USA) as per manufacturer's protocol. Briefly, 5 μL of the serum samples were added to each well along with the pyruvate assay buffer, probe solution and the enzyme mix, and incubated for 30 min at RT. The absorbance was measured at 570 nm in the Synergy H4 Hybrid 96-Well Plate Reader (Biotek, VT, USA) using Gen5 software, and the concentration of the serum pyruvate levels were assessed.

Statistical analysis

Statistical analyses were performed with GraphPad Prism 9.0.2. Two-way ANOVA with Tukey's multiple comparison *post-hoc* test was utilized for all groups. An unpaired Student's *t* test was utilized when comparing only two groups. For the myofibre force-frequency data, two-way repeated-measures ANOVA (treatment × frequency), with frequency as the repeated factor was used to test for the main effect of treatment and the treatment × frequency interaction. Unless otherwise specified each black dot or square, and the red triangle represent the data obtained from a mouse. Data are expressed as mean ± SEM. The comparison-wise error rate, α,

was set at 0.05 for statistical analysis of all data analysed using GraphPad Prism 9.0.2 software (La Jolla, CA, USA), where asterisk (*) denotes significant difference from the *post-hoc* test.

Results

P7C3 treatment alleviates the fasting blood glucose, insulin resistance and glucose intolerance in db/db mice

The db-P7C3 treated mice showed a significant decrease in the fasting blood glucose levels compared with the vehicle-treated *db/db* mice, while the db-Veh mice exhibited an increase compared with WT mice (*Figure* 1A). The C57Bl/6J WT mice displayed the same amount of circulating blood glucose levels during the weekly assessment for the entire 4 weeks. These data suggest that P7C3 improves the insulin sensitivity or glucose utilization in the type 2 diabetic *db/db* mice. Circulating blood glucose levels in response to the ITT were found to be significantly reduced at all-time points analysed in db-P7C3 vs. db-Veh mice (*Figure* 1B) confirming the insulin sensitivity of the db-P7C3 treated mice. A similar response to treatment was observed for the intraperitoneal GTT (*Figure* 1C). The index of the total glucose shift calculated as per cent AUC using trapezium method also displayed a significant decrease in the circulating blood glucose levels in the db-P7C3 mice compared with db-Veh mice (*Figure* 1D). This validates that the *db/db* mice treated with P7C3 has increased glucose uptake, possibly through insulin-dependent mechanism. Subsequently, we also found that the circulating insulin levels were also increased in the db-P7C3 treated mice with decreased homeostatic model of insulin resistance (HOMA-IR) and increased β cells function (HOMA-B) compared with db-Veh mice (*Figure* 1E–G). Together, this clearly demonstrates that the intraperitoneal administration of P7C3 in the type 2 diabetic, *db/db* mice increases the glucose uptake, and promotes pancreatic β cells function.

P7C3 treatment increases the number of pancreatic β cells in db/db mice

To assess whether db-P7C3 mice improve pancreatic β cells function of the islets of Langerhans, we utilized the *db/db* mice treated with vehicle or P7C3 for 4 weeks. Immunohistochemical analysis of the pancreatic islets of Langerhans displayed a significant increase in the insulin positive β cells area per islet of Langerhans area (*Figure* 2A, B). In addition, histological analysis of the pancreatic tissue cryosections stained with Gomori trichrome also displayed a significant
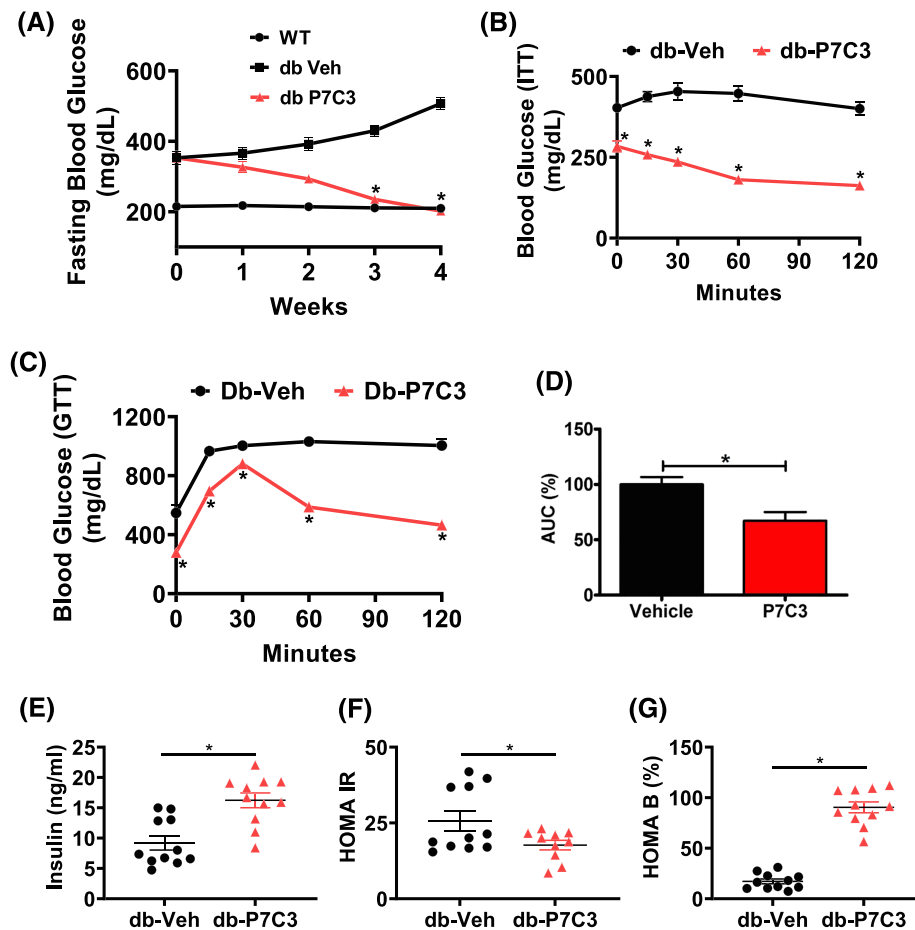
Figure 1 P7C3 reverses hyperinsulinaemia and hyperglycaemia of the diabetic mice. The 16-week-old type 2 diabetic (*db/db*) mice were administered daily with intraperitoneal dose of P7C3 (10 mg/kg/day) or vehicle for 4 weeks. (A) Weekly 6 h fasting blood glucose levels of the *db/db* mice treated with P7C3 or vehicle (*n* = 11 each), and the C57Bl/6J WT (*n* = 6) naïve control mice. (B) Insulin tolerance test (ITT) of 6 h fasted *db/db* mice injected with 1 U/kg body weight human insulin intraperitoneally (*n* = 4–5 per group). (C) Glucose tolerance test (GTT) of overnight fasted *db/db* mice injected with 2 g/kg body weight D-(+)-glucose intraperitoneally and measured with GOD-POD method (*n* = 5 mice per group). (D) The area under the curve of GTT was obtained using the trapezium method and expressed in percentage. (E) The circulating insulin levels in blood serum and (F) homeostatic model of insulin resistance (HOMA IR) and (G) homoeostatic model of pancreatic β-cells (HOMA B) expressed in percentage. Data are expressed as mean ± SEM; *$P < 0.05$; P7C3 vs. vehicle-treated *db/db* mice. The age-matched WT mice were used as naïve control to determine the baseline weekly fasting blood glucose levels.

increase in the number of β cells and islet of Langerhans per tissue section along with increased number of β cells per islets of Langerhans in the db-P7C3 mice compared with db-Veh treated mice (*Figure* 2C–F). Taken together, this clearly suggests that there is increased number of pancreatic β cells in the P7C3 treated type 2 diabetic *db/db* mice, which contributed to the increased glucose uptake in the db-P7C3 mice.

P7C3 treatment increases the physical performance of db/db mice

To determine whether P7C3 treatment modulates the physical performance in *db/db* mice, we compared fore-limb and

hind-limb grip strength and voluntary free running wheel performance, along with the *ex vivo* force frequency of the extensor digitorum longus muscle. The db-P7C3 treated mice displayed a significant increase in the fore-limb and hind-limb grip strengths compared with db-Veh treated mice (*Figure* 3A,B). The db-Veh mice also displayed a significant decrease in the fore-limb and hind-limb grip strengths compared with WT mice (supporting information, *Figure* S3A,B). There was significant group × frequency for both the absolute and normalized force frequency relationship data (*P* = 0.05 and 0.04, respectively) when comparing the WT, db-Veh, and db-P7C3 mice, although no main effect of treatment was observed for either measure of the *ex vivo* extensor digitorum longus muscle contractility. These data indicate a trend for reduced force in the db-Veh group at
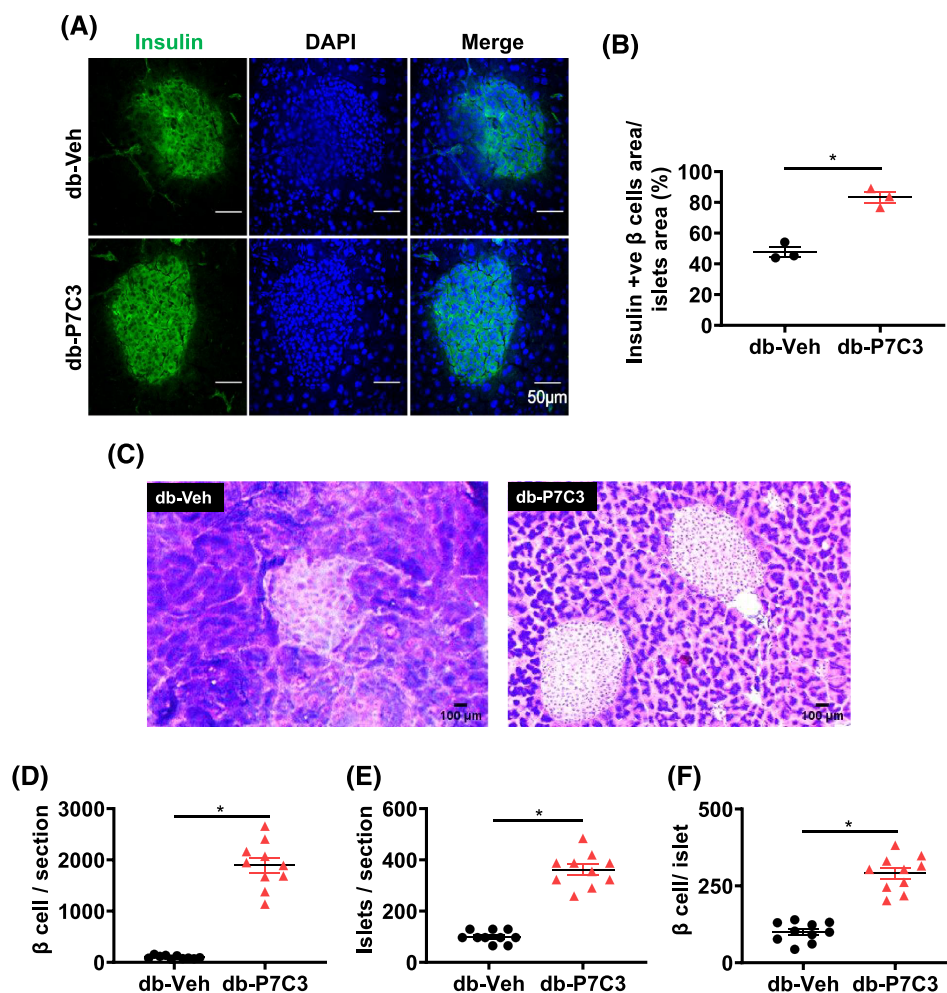
Figure 2 P7C3 increases the pancreatic β cells number and function of the *db/db* mice. (A) Immunohistochemical staining of insulin secreting pancreatic β cells (green). (B) The insulin secreting pancreatic β cells area per islet of Langerhans expressed as percentage. (C) Gomori aldehyde fuchsin staining of pancreas. (D) The number of pancreatic β cells per section, and (E) number of islet of Langerhans per section and (F) number of pancreatic β cells per islet of Langerhans. Data are expressed as mean ± SEM; *$P < 0.05$; P7C3 vs. vehicle-treated *db/db* mice.

higher frequencies, which is mitigated in the db-P7C3 group (*Figure* 3C,D). However, analysis of the area under curve through the trapezium method displayed a significant increase in the absolute myofibre force frequency in db-P7C3 mice compared with db-Veh treated mice (*Figure* 3E). The db-Veh mice also displayed a significant decrease in the absolute myofibre force frequency area under curve compared with WT mice (*Figure* S3C). The normalized myofibre force frequency also showed a similar increase in the db-P7C3 treated mice (*Figure* 3F). Even though the db-Veh mice displayed a decrease in the normalized myofibre force frequency area under curve compared with WT mice, it was found to be non-significant (*Figure* S3D). In addition, the voluntary running wheel performance of the db-P7C3 treated mice also displayed a significant increase in the distance covered compared with db-Veh treated mice (*Figure* 3G). Together, these data suggest that

P7C3 treatment increases the physical performance of the type 2 diabetic *db/db* mice.

P7C3 treatment ameliorates the diabetic skeletal muscle phenotype of the db/db mice

We then sought to measure the myofibre size of the type 2 diabetic *db/db* mice treated with vehicle or P7C3. Histological analysis of the haematoxylin and eosin (H&E) stained tibialis anterior muscle cross-sectional area around the mid-belly region displayed muscle atrophy with increased number of smaller (0–1500 μm^2) myofibres cross-sectional areas in db-Veh treated mice compared with WT and db-P7C3 treated mice (*Figure* 4A–C). The C57Bl/6J WT mice showed decreased number of small (0–1500 μm^2) myofibres and increased number of medium (1500–3000 μm^2) and larger (>3000 μm^2)
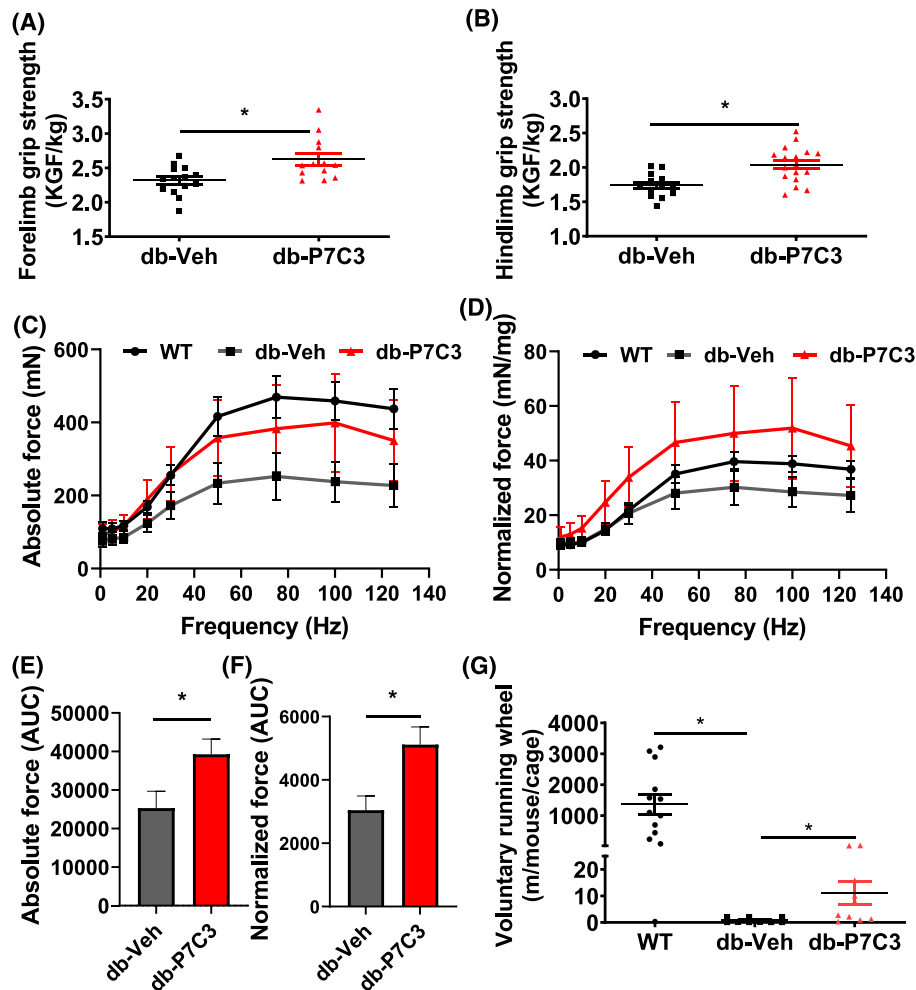
Figure 3 P7C3 enhances physical performance of *db/db* mice. (A) Fore-limb grip strength and (B) hind-limb grip strength measured and expressed as KGF/kg body weight. (C) The absolute force frequency and (D) normalized force frequency of the extensor digitorum longus muscles. (E) The area under the curve of the absolute muscle force frequency and (F) the normalized muscle force frequency. (G) The voluntary running wheel performance of the mice expressed in metres. Data are expressed as mean ± SEM; *$P < 0.05$; P7C3 vs. vehicle-treated *db/db* mice. The age-matched WT mice were used as naïve control to determine the baseline muscle force frequencies of the extensor digitorum longus muscle.

myofibres cross-sectional areas (*Figure* 4C). Noticeably, the db-P7C3 treated mice displayed a significant decrease in the small myofibres cross-sectional areas compared with the db-Veh treated mice, with a shift towards an increase in medium and larger sized myofibres cross-sectional areas (*Figure* 4A–C). There was also a significant increase in the medium-sized myofibres and decrease in larger sized myofibres in the db-Veh treated mice compared with the WT mice (*Figure* 4C). Subsequent transmission electron microscopy (TEM) image analysis of the longitudinal sections of the extensor digitorum longus muscles also displayed a significant decrease in the myofibre diameter in the db-Veh treated mice compared with the WT mice (*Figure* 4D,E). Similar to the H&E-stained tibialis anterior muscle cryosections, the TEM images of the db-P7C3 treated mice also displayed an increase in the myofibre diameter of the extensor digitorum longus muscle compared with the db-Veh treated EDL muscle. However,

it was found to be significantly lower than the WT mice (*Figure* 4E). Interestingly, the TEM images also displayed increased mitochondrial area in the db-Veh treated mice compared with WT and db-P7C3 treated mice (*Figure* 4D,F). To assess the metabolic status and mitochondrial function in the skeletal muscle the SDH staining was performed. *Figure* 4G,H shows the decrease in the SDH activity in db-Veh mice compared with WT, whereas treatment with P7C3 for 4 weeks significantly improved the SDH positive myofibres in db-P7C3 mice skeletal muscle. To gain further insight into the mitochondrial DNA (mtDNA) content, *16S* expression was measured. *Figure* 4I shows the increased expression of mtDNA in db-Veh compared with WT ($P = 0.06$), whereas, the *16S* expression was significantly decreased in db-P7C3 group compared with db-Veh mice. Together, this suggests that P7C3 treatment rescues the type 2 diabetic skeletal muscle phenotype of the *db/db* mice with an increase in the myofibre size

(A)

(B)

(C)

(D)

(E)

(F)

(G)

(H)

(I)
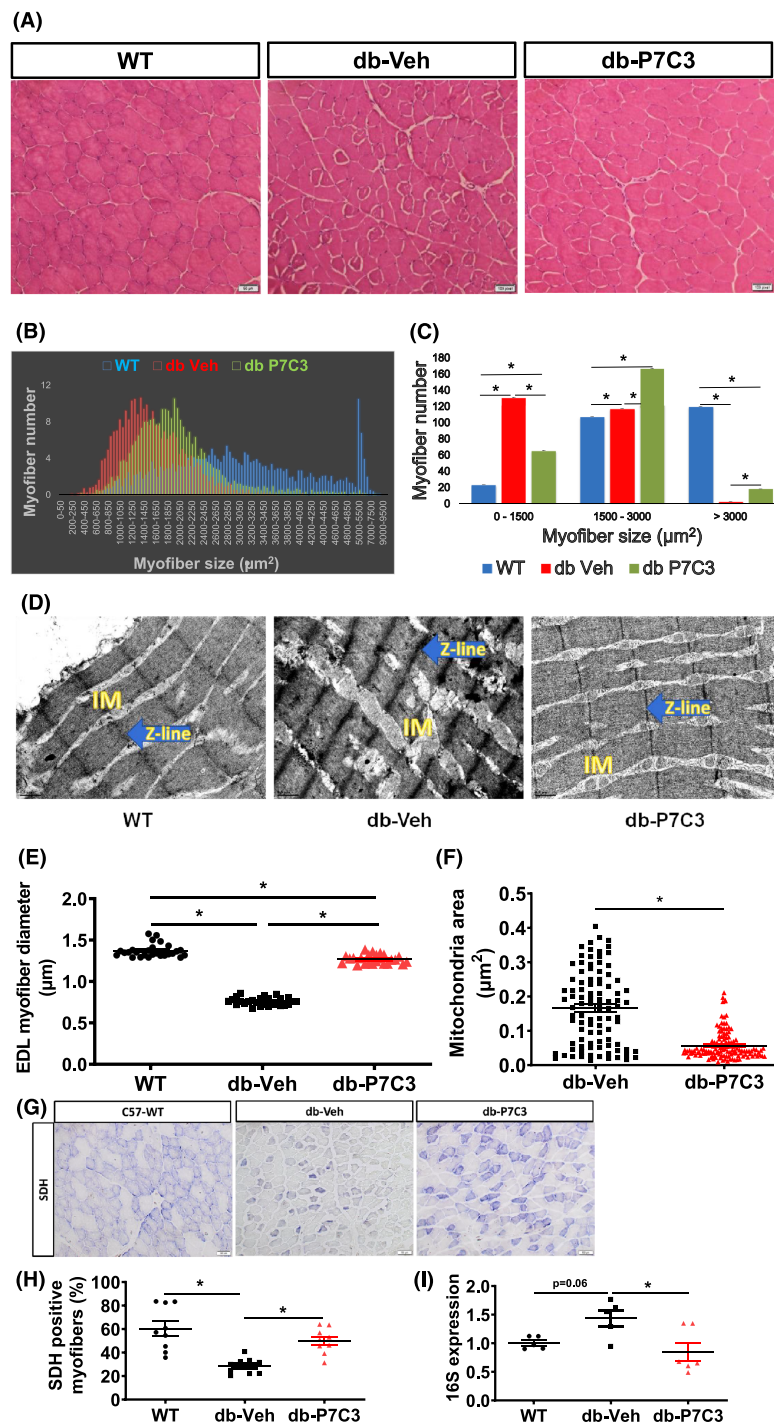
Figure 4 P7C3 ameliorates the diabetic skeletal muscle phenotype of the *db/db* mice. (A) Haematoxylin and eosin stained ×20 magnification images of the tibialis anterior muscles of the diabetic mice treated with vehicle or P7C3 and the wild-type naïve control mice. (B,C) analysis of 250 random myofibres cross-sectional area of the haematoxylin and eosin-stained images per section and 3 such section was counted per mice, where $n = 3$ mice per group displaying a shift towards medium-sized myofibres in the db-P7C3 treated mice (green) compared to db-Veh treated mice (red). The age-matched WT naïve control mice myofibres display an increased larger sized myofibres (blue). (D) Transmission electron microscopy images of the extensor digitorum longus muscle of the WT naïve control, db-Veh and db-P7C3 treated mice. The intermyofibrillar mitochondria (IM), and the Z-lines (blue arrows) are distinguished in the TEM images taken at ×30 000 magnification. (E) Analysis of the extensor digitorum longus muscles myofibre diameter of TEM images at ×30 000 magnifications ($n = 8$–9 myofibres per image, and 3 such images were analysed per group). Data are expressed as mean ± SEM; *$P < 0.05$. (F) Mitochondrial area measured from db-Veh or db-P7C3 expressed as μm^2. (G) Succinate dehydrogenase (SDH) staining of TA muscle, (H) quantification of SDH stained myofibres, and (I) relative mRNA expression of *16S* in wild-type (WT), db-Veh, and db-P7C3. Data are expressed as mean ± SEM, $P < 0.05$.
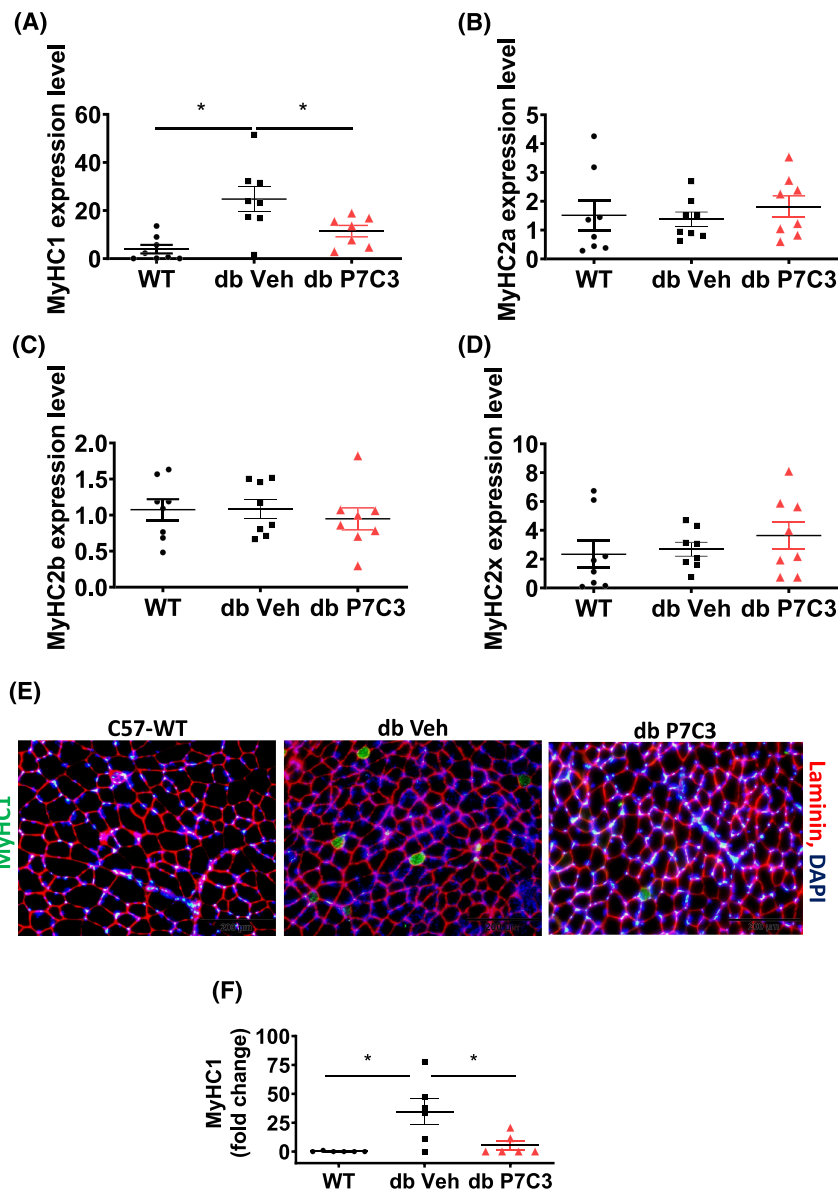
Figure 5 P7C3 decreases MyHC1 expression levels and immunostained myofibres numbers in gastrocnemius muscle. Relative gene expression levels of myosin heavy chain fibre types: (A) *MyHC1*, (B) *MyHC2a*, (C) *MyHC2b*, and (D) *MyHC2x*. (E) Immunolabelling of tibialis anterior muscle cryosections of WT, db-Veh, and db-P7C3 treated mice. MyHC1 positive myofibres are immunostained in green, laminin in red and DAPI for nuclei in blue. (F) Quantification of MyHC1 depicting the fold change in green myofibre immunostaining. Data are expressed as mean ± SEM; *$P < 0.05$. The age-matched WT mice was used as naïve control to determine the baseline expression levels of the myosin heavy chain fibre types in gastrocnemius muscle and immunostaining of MyHC1 in tibialis anterior muscle.

and SDH positive myofibres, along with reduced mitochondrial copy number likely due to decreased stress resulting in improved mitochondrial structure and function.

P7C3 treatment decreases MyHC1 expression and number in db/db mice

We next sought to determine the myofibre types in the db-P7C3 treated mice due to the observed shift in myofibre size. The db-P7C3 treated mice displayed a significant decrease in the MyHC type 1 (*MyHC1*) expression levels in the gastrocnemius muscle compared with the db-Veh mice (*Figure* 5A). Moreover, the *MyHC1* expression levels were found to be non-significant between the WT and db-P7C3 treated mice. In agreement with other finding, we found a many-fold increase in the expression levels of *MyHC1* in the db-Veh treated mice compared with WT mice, suggestive of an alternative increased slow oxidative metabolism in the diabetic mice.[34] Further, qPCR analysis of the

db-P7C3 mice gastrocnemius muscle for myosin heavy chain fibre types, that is, *MyHC*-2a, *MyHC*-2b, and *MyHC*-2x displayed no significant change in their expression levels compared with db-Veh treated mice and the WT mice (*Figure* 5B–D). Subsequent analysis of the immunostained tibialis anterior muscle cryosections displayed a significant decrease in the number of MyHC1 positive myofibres in the db-P7C3 treated mice compared with db-Veh treated mice, which was found to be non-significant compared with the WT mice (*Figure* 5E,F). These data suggest that the diabetic skeletal muscle phenotype of *db/db* mice is rescued by P7C3 treatment with a decrease in the slow oxidative myofibres.

P7C3 treatment enhances mitochondrial fatty acid oxidation and decreases the myofibre stress in the db/db mice

Given that P7C3 treatment rescued the diabetic skeletal muscle phenotype of the *db/db* mice we next examined a panel of metabolic markers through qPCR gene expression analysis of the gastrocnemius muscle. We found that the key genes involved in fatty acid uptake (*Fabp1* and *CD36*) to be significantly down-regulated in the db-P7C3 treated mice compared with db-Veh treated mice, while there was no significant difference between the db-P7C3 and WT mice (*Figure* 6A,B). Whereas, the expression levels of key genes involved in fatty acid oxidation (*Pdk4* and *Cpt1*) was found to significantly up-regulated in db-P7C3 treated mice compared to both db-Veh treated mice and the C57Bl/6J naïve control mice (*Figure* 6C,D). Noticeably, the db-P7C3 treated mice also resulted in a significant reduction in the expression level of *Fgf21*, the stress-induced myokine compared with the db-Veh treated mice, while it was non-significant compared with the WT mice (*Figure* 6E). To evaluate the treatment responsive genes in diabetic skeletal muscle, RNA-seq analysis was performed. *Figure* 6G shows heat map with significant key differentially expressed genes in the db-P7C3 group compared with db-Veh. The key genes include increased *Ppargc1a* (PGC1a), decreased inflammation or stress responses along with improved myogenic genes with P7C3 treatment. As shown in the Venn diagram and Volcano plot *Figure* 6H,I, respectively, the RNA-seq analysis showed high number of treatment responsive genes with 772/1415 genes up-regulated along with 1213/1726 genes down-regulated. We identified significant pathways that are up-regulated due to P7C3 treatment, which include muscle structure development, metabolic pathways involved in energy metabolism (NADH, pyruvate, and ATP), calcium signalling, and glycolysis and gluconeogenesis. The pathways that are significantly down-regulated include inflammation (NFkB, IL-6,8, TNF, and cytokine production), TLR signalling, TGF-β, apoptotic and cell cycle processes, fatty acid elonga-

tion, and cytokine receptor and NADPH oxidase activity (*Figure* 6J). Taken together, this suggest that P7C3 treatment of the type 2 diabetic *db/db* mice increases mitochondrial fatty acid β-oxidation and thereby enhancing insulin sensitivity and energy metabolism of diabetic skeletal muscle phenotype with decreased oxidative stress and inflammation (*Figure* 6F,G).

P7C3 treatment increases the circulating HDL levels and decreases the inflammatory lipid mediators of the db/db mice

We next sought to determine the circulating levels of HDL and LDL/VLDL lipoproteins in blood plasma and the LC–MS/MS-based skeletal muscle lipid mediators. The db-P7C3 treated mice displayed a significant increase in the HDL lipoproteins level compared with the db-Veh treated mice (*Figure* 7A). Furthermore, the db-P7C3 treated mice also displayed a significant decrease in the LDL/VLDL lipoproteins level compared with the db-Veh treated mice (*Figure* 7B). Based on the increase in lipids in the obesogenic diabetic model, we further evaluated the lipids signalling in the skeletal muscle. The omega-6 polyunsaturated fatty acid (n-6 PUFA) arachidonic acid (AA) and its derivatives 11-HETE, 15-HETE, were significantly increased in db-Veh treated group, while P7C3 treatment of the *db/db* mice significantly attenuated the pro-inflammatory LMs in the gastrocnemius muscle. Additionally, P7C3 treatment of the diabetic mice also lowered the levels of the anti-inflammatory LMs, (n-3 PUFA) docosahexaenoic acid (DHA) and its derivatives, 7-HDoHE, 13-HDoHE, 16-HDoHE, 17-HDoHE, 20-HDoHE, and the eicosapentaenoic acid (EPA) and its derivative 5-HEPE and allowed the muscle to recover and bring the levels closer to that of the WT mice (*Figure* 7C–F). Interestingly, the levels of endocannabinoid, 2-arachidonoyl glycerol (2-AG) was found to be significantly decreased in the db-P7C3 mice compared with the db-Veh treated mice, while it was more similar to the WT mice (*Figure* 7G). However, anandamide (AEA) was found to be significantly higher in the db-P7C3 treated mice compared with the db-Veh and the WT mice (*Figure* 7H). To verify the inflammatory cytokines/chemokines, we assessed the interferon γ-induced protein 10 (IP-10/C-X-C motif chemokine ligand 10), a key pro-inflammatory target in serum using Luminex-Magpix magnetic bead immunoassay. As shown in *Figure* 7I, we detected increased IP-10 levels in db-Veh group compared with WT, whereas treatment of diabetic mice with P7C3 led to significant decrease in IP-10 levels compared with db-Veh, while it was still high compared with WT mice. To provide an in-depth analysis and overview of the gene network and pathways that are activated with P7C3 treatment in diabetic skeletal muscle the STRING network analysis was performed (*Figures* S1 and S2). The data show that the glycolytic, myogenesis, and NADH pathways
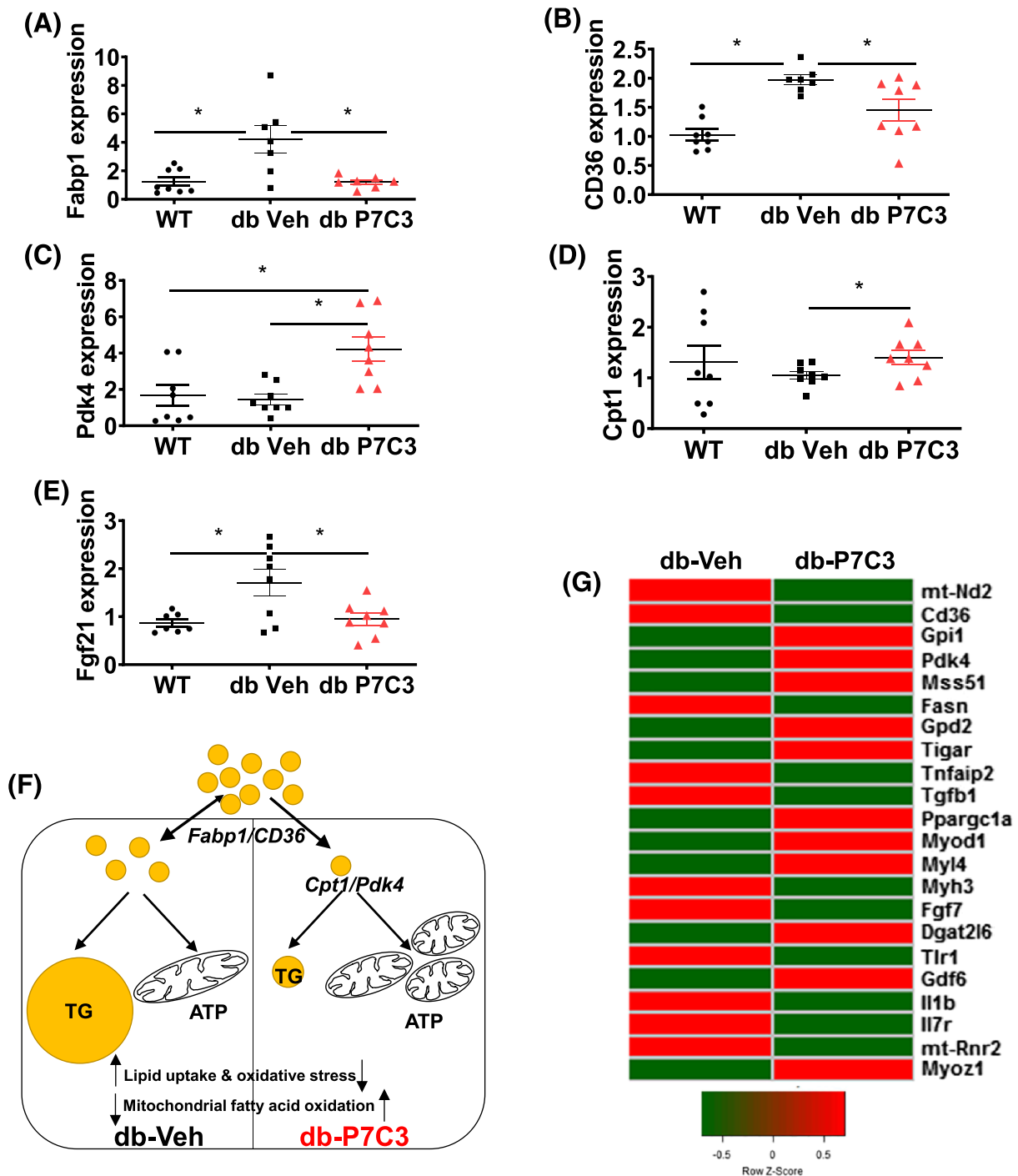
Figure 6 P7C3 treatment increases fatty acid oxidation and decrease myofibre stress in *db/db* mice. Relative mRNA expression levels of (A) *Fabp1*, (B) *CD36*, (C) *Pdk4*, (D) *Cpt1*, (E) *Fgf21*, and (F) schematic depiction of differential gene responses in db-P7C3 and db-Veh showing increased mitochondrial fatty acid oxidation and decreased fatty acid uptake and oxidative stress with P7C3 treatment in diabetic mice (G) RNA-seq analysis of skeletal muscle from db-Veh and db-P7C3 *(H)* volcano plot showing differentially expressed genes (DEG) in db_P7C3-db_Veh. The up-regulated genes (red), and the down-regulated genes (green) with a fold change <0.6, and with $P < 0.05$ (I) Venn diagram showing comparison of the differentially up-regulated genes in db_P7C3-db_Veh and down-regulated genes in db_Veh-WT_Veh, and provides the P7C3 treatment responsive genes with 772 genes up-regulated and 1213 genes down-regulated, respectively (J) the top 17 up-regulated and 16 down-regulated pathways in the biological processes (BPs), chemical component (CC), Kyoto encyclopaedia of genes and genomes (KEGG) and molecular function (MF) pathways. Data expressed is mean ± SEM, *$P < 0.05$. The age-matched WT mice was used as naïve control to determine the baseline expression levels of the key genes involved in fatty acid uptake, oxidation, and oxidative stress in gastrocnemius muscle.
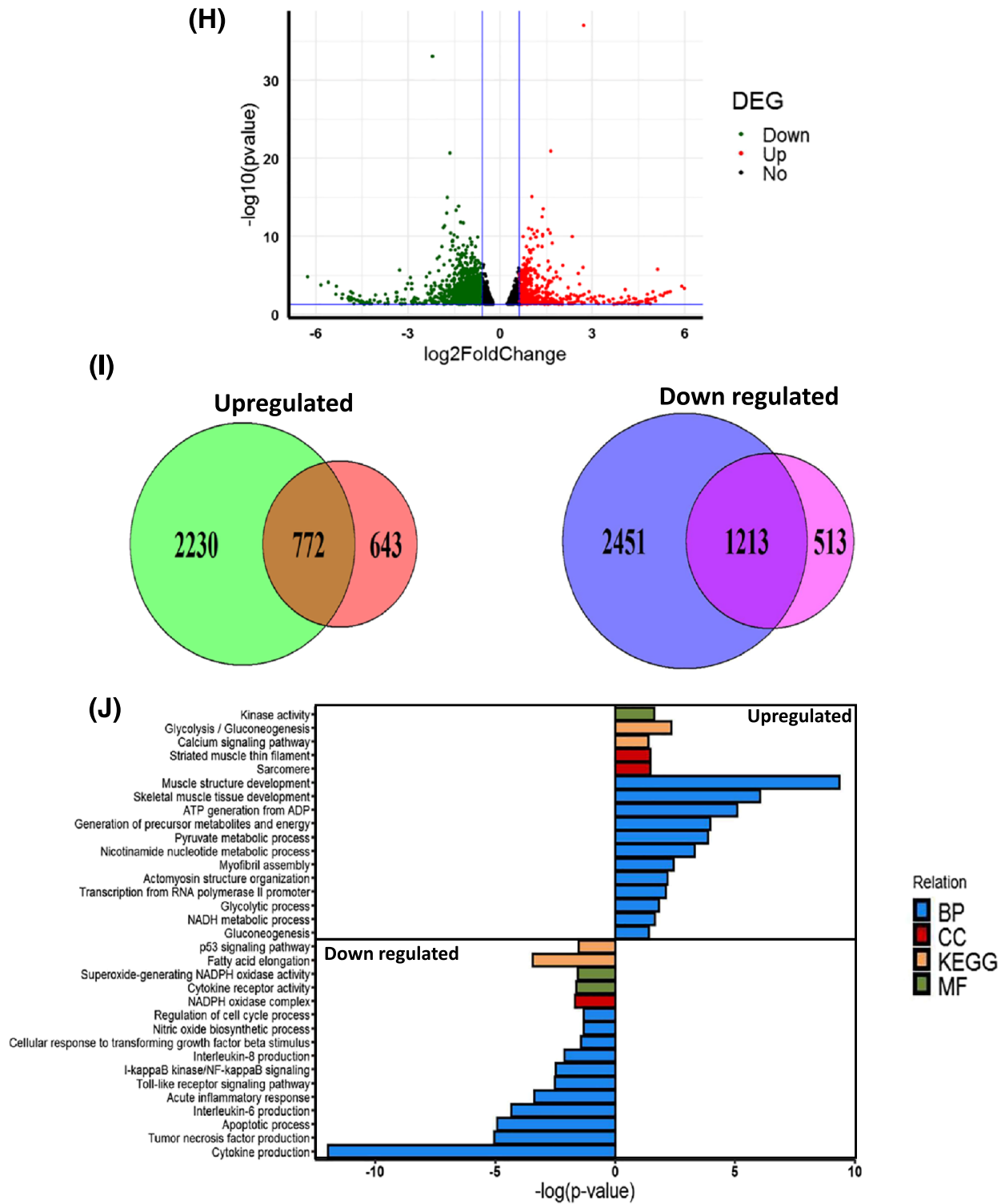
Figure 6 Continued
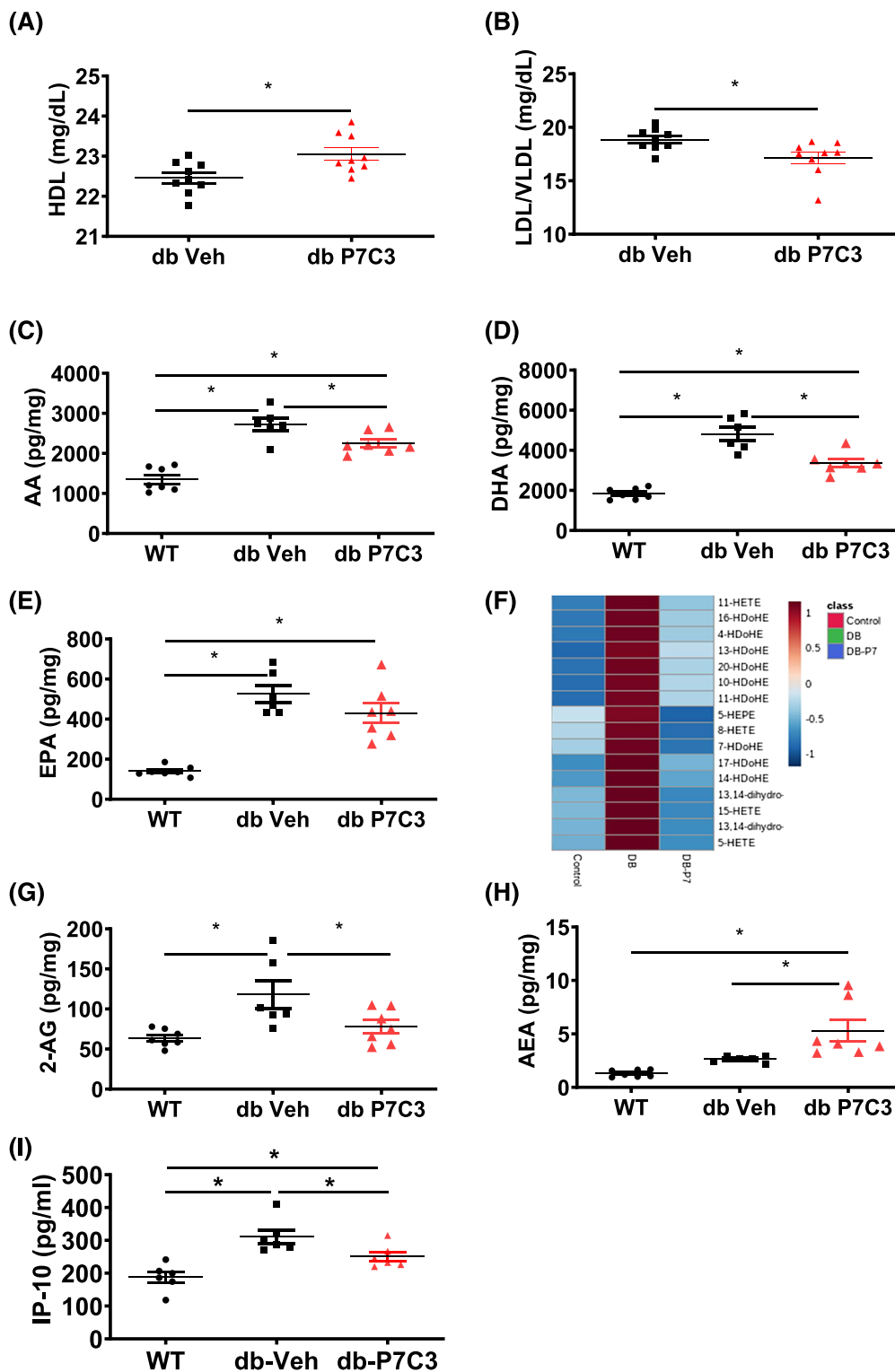
Figure 7 Cholesterol and lipid mediators are differentially altered in P7C3 treated *db/db* mice. (A) high-density lipoprotein, (B) low-density lipoprotein/very low-density lipoprotein ratio. Panels (C–H) lipid mediators measured in wild-type (WT), db-Veh and db-P7C3 treated mice, where (C) arachidonic acid; AA, (D) docosahexaenoic acid; DHA, (E) Eicosapentaenoic acid; EPA, (F) heat map of the pro-inflammatory AA derivatives HETEs, and the anti-inflammatory DHA derivatives HDoHEs and the EPA derivative HEPE (G) endocannabinoids, 2-arachidonoylglycerol; 2-AG and (H) anandamide; AEA. (I) Levels of serum IP-10 (C-X-C motif chemokine ligand 10) measured by Luminex-MagPix magnetic bead immunoassay. Data are expressed as mean ± SEM; *$P < 0.05$. The age-matched WT mice were used as naïve control to determine the baseline lipid mediators levels in gastrocnemius muscle.
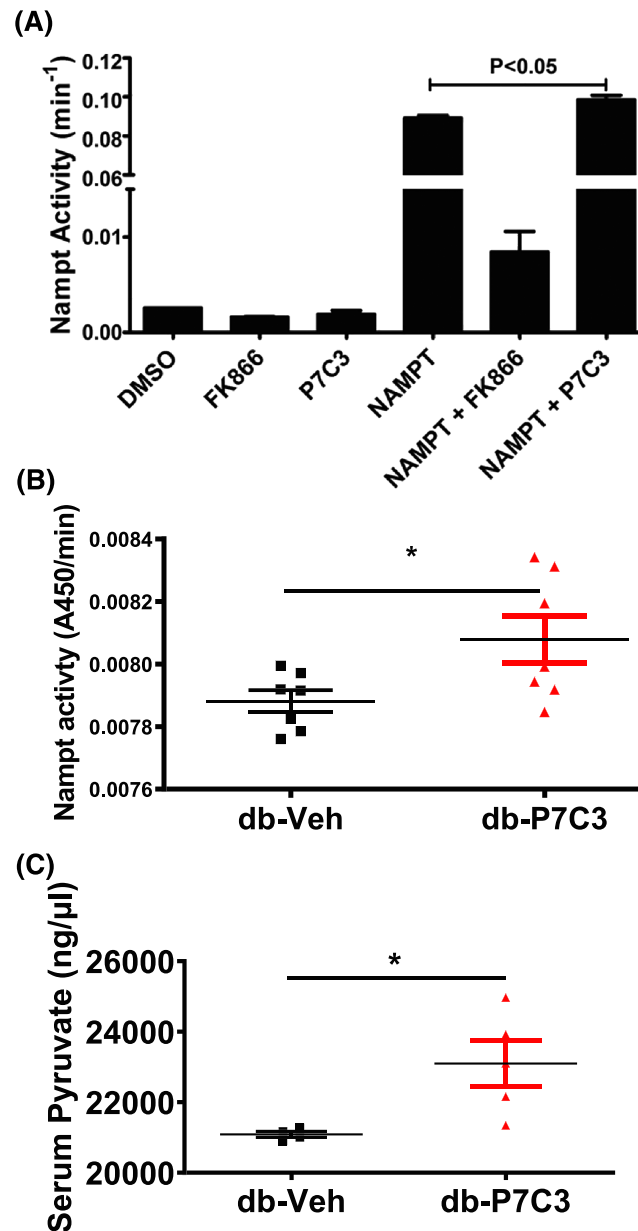
Figure 8 P7C3 treatment improves the Nampt enzymatic activity. (A) Enzymatic activity of recombinant Nampt was measured every 5 min for 1 h. Negative control (DMSO), positive control (Nampt enzyme), Nampt inhibitor (FK866), and Nampt activator (P7C3) were all utilized to assess the enzymatic activity. (B) The gastrocnemius muscle Nampt enzymatic activity was measured every 5 min for a total duration of 40 min. Data are expressed as mean ± SEM; *$P < 0.05$ of the absorbance measured at 20 min during the linear range. (C) Serum pyruvate activity of db-Veh and db-P7C3 treated mice. Data expressed as mean ± SEM with $P < 0.05$.

were up-regulated, whereas the inflammation, apoptosis and stress responsive genes are down-regulated. Furthermore, TNFα expression was detected at high levels in db-Veh compared with db-P7C3 skeletal muscle (*Figure* S3E). Overall, these data suggest that P7C3 treatment of the diabetic mice improves the circulating good lipoproteins and lipid mediators of the lipoxygenase (LOX) pathway (*Figures* S1–S5) and contribute towards skeletal muscle recovery from the chronic low-grade inflammation associated with obesity and diabetes.

P7C3 treatment enhances the Nampt activity both *in vitro* and *in vivo*

Recent report show that administration of P7C3 in animal models and tissue cultures enhance the enzymatic activity of Nampt, the key rate-limiting enzyme in the NAD salvage pathway from nicotinamide.[35] Therefore, we tested the P7C3 specificity of Nampt activity using enzyme assay with or without P7C (Figure 8A). As shown in Figure 8A, the Nampt

activity was found to be significantly decreased with the Nampt inhibitor (FK866) and increased with the Nampt activator (P7C3). The Nampt enzymatic activity was at its basal level and was found to be non-significant between the negative control DMSO, and the inhibitor and activator alone (Figure 8A). Furthermore, db-P7C3 treated mice displayed a significant increase in the Nampt activity in gastrocnemius muscle compared with the db-Veh treated mice (Figure 8B). In addition to Nampt activity, the levels of pyruvate in serum were assessed from diabetic mice treated with Nampt activator P7C3. As shown in Figure 8C, the serum pyruvate levels were significantly high in db-P7C3 treated mice compared with db-Veh. Together, this shows the specificity of P7C3 as the Nampt activator, and these data suggest that P7C3 administration increased Nampt activity in the type 2 diabetic *db/db* mice.

P7C3-mediated effects are Nampt-dependent

Next, to test whether the observed P7C3-mediated effects are Nampt-dependent, we utilized the Nampt heterozygous-null (Nampt$^{+/-}$) and their littermate WT mice that were administered with a single dose of 10 mg/kg body weight P7C3, i/p. The tail snip PCR analysis clearly identified the Nampt$^{+/-}$ and their littermate WT mice, with a double (300 bp and 500 bp) and a single (300 bp) intensity bands, respectively (*Figure* S6A). The fore-limb grip strength of the Nampt$^{+/-}$ mice was found to be significantly decreased compared with the littermate WT mice (*Figure* S6B). Subsequent, GTT clearly showed a significant decrease in the circulating blood glucose levels of the Nampt littermate WT mice treated with P7C3 compared with the vehicle-treated littermate WT mice. The Nampt$^{+/-}$ mice treated with P7C3 did not show any significant effect on the blood glucose levels tested at all-time points analysed compared with the vehicle-treated Nampt$^{+/-}$ mice (*Figure* S6C,D). The index of the total glucose shift was calculated as per cent AUC also displayed a significant decrease in the circulating blood glucose levels in the P7C3 treated Nampt littermate WT mice compared with vehicle-treated Nampt littermate WT mice (*Figure* S6E), with no significant differences between the P7C3 and vehicle-treated Nampt$^{+/-}$ mice (*Figure* S6F). These data demonstrate that P7C3 modulates its anti-glycaemic effect through the activation of Nampt and suggest that the amelioration of the hyperglycaemic effect and its associated skeletal muscle phenotype observed in the type 2 diabetic *db/db* mice treated with P7C3 is Nampt-dependent.

Discussion

The P7C3 is an aminopropyl carbazole that was reported as a neuroprotective compound in animal models of neurodegen-

erative diseases or nerve cell injury.[23] Recently, it has been reported that P7C3-A20 treatment of C57Bl/6J mice on a high-fat diet rescued the fatty liver syndrome with improved insulin sensitivity and hepatic inflammation.[36] P7C3 increases NAD synthesis from nicotinamide by activating Nampt, a key rate limiting enzyme in the NAD salvage pathway,[35] and analogues of P7C3 have been shown to bind to Nampt.[24] The enzymatic activity of Nampt and the bioavailability of NAD have been reported to be decreased in metabolic diseases and during ageing.[24] Currently, a multidrug approach is aimed for the treatment of diabetes, which includes skeletal muscle and other tissues in the body.[37] We hypothesized that P7C3-mediated activation of Nampt in the type 2 diabetic *db/db* mice ameliorates the diabetic skeletal muscle phenotype and improves the insulin sensitivity. In the present study, we demonstrate P7C3 as a novel compound in the amelioration of type 2 diabetic skeletal muscle phenotype and function in the Lepr^{db} homozygous-null (*db/db*) mice. Furthermore, our data provide insights into the P7C3-mediated insulin sensitivity through Nampt activation.

Based on the study, we demonstrate that the blood glucose levels of fasting blood glucose, insulin resistance, and GTTs were reduced in the db-P7C3 treated mice. Furthermore, there was increased number of pancreatic β cells and islets of Langerhans, and β cells function in the db-P7C3 treated mice. There was also increased physical performance in the db-P7C3 treated mice as measured with the fore-limb and hind-limb grip strengths, *ex vivo* myofibre force frequency and voluntary running wheel performance. Previous report identifies that doxorubicin induced decrease in NAD can be compensated by P7C3 via Nampt activity.[24] This study also shows direct cross-linking of P7C3 with recombinant Nampt enzyme. However, previous studies did not report if the observed decrease in the blood glucose levels is through direct P7C3-mediated Nampt activation, involved in NAD biosynthetic salvage pathway or due to an indirect effect. To address this question, we utilized the recombinant Nampt enzyme and assessed the Nampt enzymatic activity with P7C3 or the Nampt inhibitor FK866 *in vitro*. In addition, we also utilized the type 2 diabetic, *db/db* mice treated with P7C3 or vehicle for assessing the gastrocnemius muscle Nampt and serum pyruvate activities. We found that the Nampt enzymatic activity was increased with P7C3 and inhibited by FK866 in the *in vitro* assay, and it was also increased in the db-P7C3 treated mice. Similarly, the serum pyruvate levels were found to be increased in the db-P7C3 treated mice. To address whether the observed increase in insulin sensitivity and glucose uptake with the administration of P7C3 in the type 2 diabetic *db/db* mice is directly through Nampt activation, we utilized the Nampt$^{+/-}$ and their littermate WT mice treated once with P7C3 or vehicle for assessing the blood glucose levels of the intraperitoneal GTT. The glucose tolerance was improved in the Nampt littermate WT mice treated with P7C3 but did not improve in the

Nampt$^{+/-}$ mice treated with P7C3. This clearly indicates that the P7C3-mediated effect on glucose uptake in the type 2 diabetic *db/db* mice is via Nampt activation.

Interestingly, in the db-P7C3 treated mice there was an increase in myofibre size in hind-limb tibialis anterior and the extensor digitorum longus muscles, which shows a healthy muscle phenotype in the db-P7C3 treated mice. The type 2 diabetic *db/db* mice treated with P7C3 also displayed improved mitochondria morphology and function. The mitochondrial DNA was measured in the diabetic skeletal muscle and showed significant increase in *16S* expression, which might be due to increased oxidative stress and previous report have shown similar increase in diabetic muscle.[38] Based on P7C3 treatment, we demonstrate that *16S* expression was restored to the levels in WT muscle. More recently, P7C3 has been shown to stabilize the mitochondrial membrane potential in an *in vitro* dopaminergic cell culture model.[39] In our study, we found that P7C3 treatment of the type 2 diabetic, *db/db* mice resulted in the restoration of mitochondrial morphology and function. Furthermore, the observed shift in myofibre size from small to medium and larger myofibres was accompanied by a decrease in the MyHC1 (slow oxidative) myofibres expression levels and number, with no significant difference in the other *MyHC* fibre types expression levels in the db-P7C3 treated mice. Subsequently, we found a significant increase in the succinate dehydrogenase positive oxidative myofibres and increased *Pgc1α* expression in the db-P7C3 treated mice. Together this confirms that there is increased mitochondrial biogenesis in the P7C3 treated type 2 diabetic (*db/db*) mice that might be involved in energy metabolism.

To test this, we next looked at the expression level of the key markers in energy metabolism in gastrocnemius muscle and found decreased *Fabp1* and *CD36* expression levels along with an increase in *Pdk4* and *Cpt1* expression levels in the db-P7C3 treated mice. Strikingly, the expression level of the stress-induced myokine, *Fgf21* was found to be decreased suggestive of improved skeletal muscle health as evident in the H&E cryosections of the tibialis anterior muscle analysed for the myofibre transverse sectional areas and the TEM images of the longitudinal section of extensor digitorum longus muscle for the diameter. Together, this suggest that there is decreased fatty acid uptake and increased mitochondrial fatty acid β-oxidation along with decreased myofibre stress and inflammatory markers, including IP-10 and Tnfaip2 in the type 2 diabetic *db/db* mice treated with P7C3 for energy metabolism and tissue homeostasis of the skeletal muscle.

Low HDL and increased VLDL levels in blood are often associated with insulin resistance and type 2 diabetes, which leads to increased risk of developing cardiovascular diseases.[40–42] In this study, P7C3 treatment of the type 2 diabetic (*db/db*) mice showed a significant increase in the circulating levels of HDL along with a decrease in LDL/VLDL levels in blood. Further-

more, excess lipid accumulation in skeletal muscle is well known to cause muscle inflammation, and their levels have been reported to be increased in type 2 diabetic and obese individuals and animal models.[43–46] In this study, we found an increase in the long chain poly-unsaturated fatty acids (LC-PUFA), especially the arachidonic acid (AA, 20:4; n-6), docosahexaenoic acid (DHA, 22:6; n-3) and eicosapentaenoic acid (EPA, 20:5; n-3) and their derivatives HETE, HDoHE and HEPE of the lipoxygenase (LOX) pathway through LC–MS/MS lipidomics of gastrocnemius muscle of the type 2 diabetic (*db/db*) mice. Intriguingly, the db-P7C3 treated mice significantly decreased the levels of AA, DHA and EPA, and their derivatives in gastrocnemius muscle, suggestive of decreased muscle inflammation in the db-P7C3 treated mice. The arachidonic acid is also known to serve as a precursor for eicosanoids and endocannabinoids, and the most studied endocannabinoids are 2-arachidonoyl glycerol (2-AG) and anandamide (AEA). P7C3 treatment of the type 2 diabetic (*db/db*) mice also resulted in a decrease in 2-AG levels consistent with the AA levels in these mice. However, there was an increase in the AEA levels in the db-P7C3 treated mice, the significance of which is not known and could be involved in the neuromuscular junction. The increase in HDL cholesterol in the db-P7C3 treated mice might contribute to the cardioprotective effects with increased cholesterol efflux, and anti-oxidative and anti-inflammatory properties.[47] Moreover, the decrease in LDL/VLDL cholesterol levels in the db-P7C3 treated mice might also decrease atherosclerosis in heart disease, and alleviate insulin resistance and type 2 diabetes. Furthermore, the lipidomic analysis reveal that P7C3 treatment of the type 2 diabetic (*db/db*) mice attenuates the skeletal muscle inflammatory disease. In the present study, we utilized STRING network analysis and identified that key genes and clusters responsible for muscle development, calcium signalling, glycolysis and gluconeogenesis were up-regulated, whereas, the inflammatory genes, cytokine production and apoptotic genes were down-regulated (*Figures* S1 and S2; Data S1). In line with the present findings, a previous report shows similar increase in inflammatory markers using human myocytes from type 2 diabetic individuals with dysregulated myogenesis and gene network associations for development of diabetes.[48] Overall, based on P7C3 treatment and in-depth RNA-Seq and network analysis we identify beneficial molecular responses that attenuate diabetes and improves muscle function.

In summary, in the present study we demonstrate that intraperitoneal administration of P7C3 in type 2 diabetic (*db/db*) mice, daily for 4 weeks improved the glucose uptake by decreasing the fasting blood glucose and insulin resistance, and increasing glucose tolerance, along with increased number of pancreatic β-cells, islet of Langerhans, and β cells function. The P7C3 treatment also improved the physical performance (fore-limb and hind-limb grip strengths, *ex vivo* myofibre force frequency and the voluntary free running

wheel performance) alleviating the diabetic muscle pheno-type of the *db/db* mice. Subsequent, histological analysis of the hind-limb tibialis anterior and extensor digitorum longus muscles displayed an increase in the myofibre size, with a si-multaneous decrease in both *MyHC1* expression levels and immunostaining of the slow oxidative myofibres in the db-P7C3 treated mice. The transmission electron microscopy also revealed an improved mitochondrial morphology in the db-P7C3 treated mice, probably with improved mitochondrial membrane potential. The increased SDH positive myofibres and *Pgc*-1α expression in the db-P7C3 treated mice demon-strate improved mitochondrial function. Mechanistically, there was increased mitochondrial fatty acid β-oxidation with decreased fatty acid uptake and oxidative stress in the db-P7C3 treated mice in energy metabolism. RNA Seq analy-sis also displayed an increase in fatty acid oxidation, mito-chondrial biogenesis, muscle function with reduced inflammation. The LC–MS/MS lipidomic analysis of gastrocne-mius muscle also displayed a decrease in the inflammatory lipids, along with an increase in the circulating HDL and de-crease in the VLDL/LDL lipids in the db-P7C3 treated mice resulting in reduced muscle inflammation. The serum pro-inflammatory marker IP-10 levels also displayed a de-crease in db-P7C3 treated mice. The specificity of P7C3 treat-ment was confirmed with an increase in the Nampt activity both *in vitro* and *in vivo*. The GTT of the P7C3 treated Nampt$^{+/-}$ mice further validated the hyperglycaemic effects of P7C3 as Nampt-mediated. Together, our findings highlight the importance of P7C3-mediated Nampt activation in ame-liorating the diabetic skeletal muscle phenotype of *db/db* mice and Nampt actvator P7C3 as a potential treatment strat-egy in type 2 diabetes.

Conflict of interest

The authors declare that there is no conflict of interest.

Disclosures

Patent awarded to USF: US Patent 11,007,178, 2021. USF Pro-visional patent filed: 19A039PR.

Online supplementary material

Additional supporting information may be found online in the Supporting Information section at the end of the article.

References

1. Wojciechowska J, Krajewski W, Bolanowski M, Kręcicki T, Zatoński T. Diabetes and cancer: a review of current knowledge. *Exp Clin Endocrinol Diabetes* 2016;**124**: 263–275.
2. Phielix E, Mensink M. Type 2 diabetes mellitus and skeletal muscle met-abolic function. *Physiol Behav* 2008;**94**: 252–258.
3. Galicia-Garcia U, Benito-Vicente A, Jebari S, Larrea-Sebal A, Siddiqi H, Uribe KB, et al. Pathophysiology of type 2 diabetes mellitus. *Int J Mol Sci* 2020;**21**. https://doi.org/10.3390/ijms21176275
4. Twig G, Zucker I, Afek A, Cukierman-Yaffe T, Bendor CD, Derazne E, et al. Adolescent obesity and early-onset type 2 diabetes. *Diabetes Care* 2020;**43**:1487–1495.
5. Mesinovic J, Zengin A, De Courten B, Ebeling PR, Scott D. Sarcopenia and type 2 diabetes mellitus: a bidirectional rela-tionship. *Diab Metab Syndr Obes* 2019;**12**: 1057–1072.

6. Williams R, Van Gaal L, Lucioni C. Assessing the impact of complications on the costs of type II diabetes. *Diabetologia* 2002;**45**:S13–S17.
7. Liu L, Simon B, Shi J, Mallhi AK, Eisen HJ. Impact of diabetes mellitus on risk of cardiovascular disease and all-cause mortality: evidence on health outcomes and antidiabetic treatment in United States adults. *World J Diabetes* 2016;**7**:449–461.
8. Bianchi L, Volpato S. Muscle dysfunction in type 2 diabetes: a major threat to patient's mobility and independence. *Acta Diabetol* 2016;**53**:879–889.
9. Manickam R, Duszka K, Wahli W. PPARs and microbiota in skeletal muscle health and wasting. *Int J Mol Sci* 2020;**21**:https://doi.org/10.3390/ijms21218056
10. Ryder JW, Gilbert M, Zierath JR. Skeletal muscle and insulin sensitivity: pathophysi-ological alterations. *Front Biosci* 2001;**6**: D154–D163.
11. Tenenbaum A, Motro M, Schwammenthal E, Fisman EZ. Macrovascular complications

of metabolic syndrome: an early interven-tion is imperative. *Int J Cardiol* 2004;**97**: 167–172.
12. Jensen J, Rustad PI, Kolnes AJ, Lai YC. The role of skeletal muscle glycogen breakdown for regulation of insulin sensitivity by exercise. *Front Physiol* 2011;**2**:112.
13. Hegarty BD, Furler SM, Ye J, Cooney GJ, Kraegen EW. The role of intramuscular lipid in insulin resistance. *Acta Physiol Scand* 2003;**178**:373–383.
14. Lowell BB, Shulman GI. Mitochondrial dysfunction and type 2 diabetes. *Science* 2005;**307**:384–387.
15. de Guia RM, Agerholm M, Nielsen TS, Consitt LA, Søgaard D, Helge JW, et al. Aerobic and resistance exercise training reverses age-dependent decline in NAD$^+$ salvage capacity in human skeletal muscle. *Physiol Rep* 2019;**7**:e14139. https://doi.org/10.14814/phy2.14139
16. Yoshino J, Mills KF, Yoon MJ, Imai S. Nicotinamide mononucleotide, a key

NAD$^+$ intermediate, treats the pathophysiology of diet- and age-induced diabetes in mice. *Cell Metab* 2011;**14**:528–536.

17. Garten A, Schuster S, Penke M, Gorski T, de Giorgis T, Kiess W. Physiological and pathophysiological roles of NAMPT and NAD metabolism. *Nat Rev Endocrinol* 2015;**11**: 535–546.

18. Alshahrani A, AlDubayee M, Zahra M, Alsebayel FM, Alammari N, Alsudairy F, et al. Differential expression of human *N*-alpha-acetyltransferase 40 (hNAA40), nicotinamide phosphoribosyltransferase (NAMPT) and sirtuin-1 (SIRT-1) pathway in obesity and T2DM: modulation by metformin and macronutrient intake. *Diab Metab Syndr Obes* 2019;**12**:2765–2774.

19. Hallschmid M, Randeva H, Tan BK, Kern W, Lehnert H. Relationship between cerebrospinal fluid visfatin (PBEF/Nampt) levels and adiposity in humans. *Diabetes* 2009;**58**:637–640.

20. Revollo JR, Körner A, Mills KF, Satoh A, Wang T, Garten A, et al. Nampt/PBEF/visfatin regulates insulin secretion in beta cells as a systemic NAD biosynthetic enzyme. *Cell Metab* 2007;**6**:363–375.

21. Frederick DW, Loro E, Liu L, Davila A Jr, Chellappa K, Silverman IM, et al. Loss of NAD homeostasis leads to progressive and reversible degeneration of skeletal muscle. *Cell Metab* 2016;**24**:269–282.

22. Agerholm M, Dall M, Jensen BAH, Prats C, Madsen S, Basse AL, et al. Perturbations of NAD$^+$ salvage systems impact mitochondrial function and energy homeostasis in mouse myoblasts and intact skeletal muscle. *Am J Physiol Endocrinol Metab* 2018; **314**:E377–e95.

23. Pieper AA, Xie S, Capota E, Estill SJ, Zhong J, Long JM, et al. Discovery of a proneurogenic, neuroprotective chemical. *Cell* 2010;**142**:39–51.

24. Wang G, Han T, Nijhawan D, Theodoropoulos P, Naidoo J, Yadavalli S, et al. P7C3 neuroprotective chemicals function by activating the rate-limiting enzyme in NAD salvage. *Cell* 2014;**158**:1324–1334.

25. Kim W, Doyle ME, Liu Z, Lao Q, Shin YK, Carlson OD, et al. Cannabinoids inhibit insulin receptor signaling in pancreatic β-cells. *Diabetes* 2011;**60**:1198–1209.

26. Badole SL, Bodhankar SL. Antidiabetic activity of cycloart-23-ene-3beta, 25-diol (B2) isolated from Pongamia pinnata (L. Pierre) in streptozotocin-nicotinamide

induced diabetic mice. *Eur J Pharmacol* 2010;**632**:103–109.

27. Chapalamadugu KC, Panguluri SK, Bennett ES, Kolliputi N, Tipparaju SM. High level of oxygen treatment causes cardiotoxicity with arrhythmias and redox modulation. *Toxicol Appl Pharmacol* 2015;**282**:100–107.

28. Chapalamadugu KC, Tur J, Badole SL, Kukreja RC, Brotto M, Tipparaju SM. Physiological role of Kvβ2 (AKR6) in murine skeletal muscle growth and regulation. *Acta Physiol (Oxf)* 2018;**224**:e13083, https://doi.org/10.1111/apha.13083

29. Shen Z, Chen Q, Ying H, Ma Z, Bi X, Li X, et al. Identification of differentially expressed genes in the endothelial precursor cells of patients with type 2 diabetes mellitus by bioinformatics analysis. *Exp Ther Med* 2020;**19**:499–510.

30. Cirillo E, Kutmon M, Gonzalez Hernandez M, Hooimeijer T, Adriaens ME, Eijssen LMT, et al. From SNPs to pathways: Biological interpretation of type 2 diabetes (T2DM) genome wide association study (GWAS) results. *PLoS ONE* 2018;**13**:e0193515, https://doi.org/10.1371/journal.pone.0193515

31. Bader GD, Hogue CW. An automated method for finding molecular complexes in large protein interaction networks. *BMC Bioinform* 2003;**4**:2.

32. Shochat C, Wang Z, Mo C, Nelson S, Donaka R, Huang J, et al. Deletion of SREBF1, a functional bone-muscle pleiotropic gene, alters bone density and lipid signaling in zebrafish. *Endocrinology* 2021;**162**:https://doi.org/10.1210/endocr/bqaa189

33. Marrelli MT, Wang Z, Huang J, Brotto M. The skeletal muscles of mice infected with *Plasmodium berghei* and *Plasmodium chabaudi* reveal a crosstalk between lipid mediators and gene expression. *Malar J* 2020;**19**:254.

34. Klueber KM, Feczko JD, Schmidt G, Watkins JB 3rd. Skeletal muscle in the diabetic mouse: histochemical and morphometric analysis. *Anat Rec* 1989;**225**:41–45.

35. Pieper AA, McKnight SL. Benefits of enhancing nicotinamide adenine dinucleotide levels in damaged or diseased nerve cells. *Cold Spring Harb Symp Quant Biol* 2018; **83**:207–217.

36. Hua X, Sun DY, Zhang WJ, Fu JT, Tong J, Sun SJ, et al. P7C3-A20 alleviates fatty liver by shaping gut microbiota and inducing FGF21/FGF1, via the AMP-activated pro-

tein kinase/CREB regulated transcription coactivator 2 pathway. *Br J Pharmacol* 2020;**178**:2111–2130.

37. Vitali F, Mulas F, Marini P, Bellazzi R. Network-based target ranking for polypharmacological therapies. *J Biomed Inform* 2013;**46**:876–881.

38. Antonetti DA, Reynet C, Kahn CR. Increased expression of mitochondrial-encoded genes in skeletal muscle of humans with diabetes mellitus. *J Clin Invest* 1995;**95**:1383–1388.

39. Gu C, Zhang Y, Hu Q, Wu J, Ren H, Liu CF, et al. P7C3 inhibits GSK3β activation to protect dopaminergic neurons against neurotoxin-induced cell death *in vitro* and *in vivo*. *Cell Death Dis* 2017;**8**:e2858, https://doi.org/10.1038/cddis.2017.250

40. Nordestgaard BG, Varbo A. Triglycerides and cardiovascular disease. *Lancet* 2014; **384**:626–635.

41. Siddiqi HK, Kiss D, Rader D. HDL-cholesterol and cardiovascular disease: rethinking our approach. *Curr Opin Cardiol* 2015;**30**:536–542.

42. Fruchart JC. Insulin-resistance and lipoprotein abnormalities. *Diabete Metab* 1991; **17**:244–248.

43. Pellegrinelli V, Rouault C, Rodriguez-Cuenca S, Albert V, Edom-Vovard F, Vidal-Puig A, et al. Human adipocytes induce inflammation and atrophy in muscle cells during obesity. *Diabetes* 2015;**64**:3121–3134.

44. Warfel JD, Bermudez EM, Mendoza TM, Ghosh S, Zhang J, Elks CM, et al. Mitochondrial fat oxidation is essential for lipid-induced inflammation in skeletal muscle in mice. *Sci Rep* 2016;**6**:37941.

45. Romic S, Krskova K, Olszanecki R, Balazova L, Lory V, Koricanac G, et al. Obesity- and age-related alterations in FAT/CD36 translocation and lipin-1 subcellular localization in skeletal muscle of the Zucker rats. *Gen Physiol Biophys* 2017;**36**:399–406.

46. Lee YS, Li P, Huh JY, Hwang IJ, Lu M, Kim JI, et al. Inflammation is necessary for long-term but not short-term high-fat diet-induced insulin resistance. *Diabetes* 2011;**60**:2474–2483.

47. Krauss RM. Lipids and lipoproteins in patients with type 2 diabetes. *Diabetes Care* 2004;**27**:1496–1504.

48. Väremo L, Henriksen TI, Scheele C, Broholm C, Pedersen M, Uhlén M, et al. Type 2 diabetes and obesity induce similar transcriptional reprogramming in human myocytes. *Genome Med* 2017;**9**:47.